

## High-efficiency oxygen reduction by late transition metal oxides to produce H<sub>2</sub>O<sub>2</sub>

Yue Zhang,<sup>a,b</sup> Hao Jiang,<sup>a,b</sup> Chengxu Zhang,<sup>a\*</sup> Yuebin Feng,<sup>c</sup> Hang Feng,<sup>a,b</sup>  
Sanyuan Zhu<sup>a,b</sup> and Jue Hu<sup>a,b\*</sup>

<sup>a</sup>Faculty of Metallurgical and Energy Engineering, Kunming University of Science and Technology, Kunming 650093, China

<sup>b</sup>State Key Laboratory of Complex Nonferrous Metal Resources Clean Utilization, Kunming University of Science and Technology, Kunming 650093, China

<sup>c</sup>Faculty of Science, Kunming University of Science and Technology, Kunming 650093, China

\*Corresponding authors: chxzhang@kust.edu.cn (C.Z.); hujue@kust.edu.cn (J.H.)

### Chemicals

Zinc nitrate hexahydrate (Zn(NO<sub>3</sub>)<sub>2</sub> · 6H<sub>2</sub>O, 99%), Potassium hydroxide (KOH, 95%), Sodium hydroxide (NaOH, 95%), Copper nitrate trihydrate (Cu(NO<sub>3</sub>)<sub>2</sub> · 3H<sub>2</sub>O, 99%), Oxalic acid dihydrate (C<sub>2</sub>H<sub>2</sub>O<sub>4</sub>·2H<sub>2</sub>O, AR), Nickel nitrate hexahydrate (Ni(NO<sub>3</sub>)<sub>2</sub> · 6H<sub>2</sub>O, 98%), Cupric oxide (CuO, 99.5% metals basis), Zinc oxide (ZnO, 99.8% metals basis), Nickel oxide (NiO, 99.9% metals basis), Cobalt oxide (CoO, Reagent Grade) were purchased from Aladdin Biochemical Technology Co., LTD. Ethanol anhydrous (CH<sub>3</sub>CH<sub>2</sub>OH, 99.5%), Cobalt(II) acetate tetrahydrate ((CH<sub>3</sub>COO)<sub>2</sub>Co·4H<sub>2</sub>O, 99.5%), Cerium(IV) sulfate (Ce(SO<sub>4</sub>)<sub>2</sub>, 99.95% metals basis) were purchased from Shanghai Macklin Biochemical Technology Co., Ltd. Sulfuric acid (H<sub>2</sub>SO<sub>4</sub>, 98.08%) was purchased from Chengdu Colon Chemical Co., LTD. All chemicals are used directly without further purification. Deionized water (18 MΩ cm) is used in all of the experiments.

### Characterization

Powder X-ray diffraction (XRD) pattern was obtained by using Rigaku D/MAX-2200 at 40 kV, 40 mA Cu Kα radiation. X-ray photoelectron spectroscopy (XPS) analysis of monochromatic Aluminum anode X-ray source with Mo Kα (1486.6 eV) radiation has been carried out by PHI 5500 XPS with a resolution of

0.3~0.5 eV. Ultraviolet and near-infrared diffuse reflection was collected using Shimadzu UV-3600. All XPS spectra were calibrated with the C1s peak of carbon at 284.80 eV. Field emission scanning electron microscopy (FESEM) was performed with Nona-Nano SEM 450 at 5 kV acceleration voltage. Transmission electron microscopy (TEM) and high-resolution transmission electron microscopy (HRTEM) were performed at 300 kV using Tecnai G2 TF30.

### Electrochemical measurements

Electrochemical test was carried out using a three-electrode system (CHI 760E). The reference electrode is Hg/HgO electrode, and Pt foil is used as the counter electrode, and the electrolyte solutions of  $2e^-$  ORR is 0.1 M KOH, respectively. According to Nernst equation, the reference potential is calibrated with reversible hydrogen electrode (RHE).

The electrochemical catalyst was prepared by dispersing 10 mg catalyst in mixed solution containing 50  $\mu$ l of 5 wt% Nafion solution and 950  $\mu$ l of isopropanol solution. Uniform ink was obtained by ultrasonic treatment of the above mixed solution for 1 hour. 5  $\mu$ l catalyst ink was dripped on the RRDE electrode on a glass carbon disk (0.2475 cm<sup>2</sup>). The surface of the disk electrode is allowed to dry at the room temperature. The final load was about 0.2 mg cm<sup>-2</sup>. Before each test, the electrolyte solution was saturated with N<sub>2</sub> and O<sub>2</sub>, respectively. The scanning rate of the polarization curve is 10 mV/s without IR correction. The disk potential ranges from 0 to 1.1 V vs. RHE, and the potential on the platinum ring electrode is maintained at 1.4 V vs. RHE.

The selectivity, number of transferred electrons and Faraday efficiency of H<sub>2</sub>O<sub>2</sub> are determined according to the Eq (1) and (2). As follows:

$$H_2O_2\% = \frac{200 \times I_{ring}/N}{|I_{disk}| + I_{ring}/N} \quad (1)$$

$$n = \frac{4 \times I_{disk}}{I_{disk} + I_{ring}/N} \quad (2)$$

Where  $I_{disk}$  represents disc electrode current and  $I_{ring}$  represents ring electrode current. Through RRDE electrode correction, the value of N is 0.365, which represents the collection efficiency of the ring electrode.

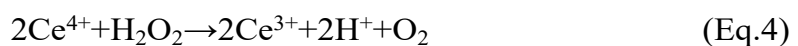
Test the Faraday efficiency and the stability of the catalyst of the actual device in batch production for a long time can be calculated by Eq (3).

$$Faradaic\ efficiency = \frac{2CVF}{Q} \quad (3)$$

Where the variables Q, V, C and F respectively represent the passing charge (C), electrolyte volume (L),  $H_2O_2$  concentration ( $mol\ L^{-1}$ ) and Faraday constant ( $96485\ C\ mol^{-1}$ ), respectively.

### **$H_2O_2$ concentration measurement and stability test**

The concentration of  $H_2O_2$  was determined in an H-type two-chamber containing a Nafion membrane, with both the cathode and anode containing 50 ml of 0.1 M KOH solution at -0.4 V vs RHE conditions, respectively. During the process of measurement, the traditional cerium sulfate method was used to determine the concentration of  $H_2O_2$ . Based on the reduction of yellow  $Ce^{4+}$  to colorless  $Ce^{3+}$ , the change of  $Ce^{4+}$  concentration before and after the reaction was measured by UV-vis spectrometry, and the maximum wavelength measured was 316 nm. 1 mM cerium sulfate solution was obtained through put 33.2 mg anhydrous cerium sulfate in 100 ml of sulfuric acid solution (0.5 M) (Eq.4). To achieve the standard curve of cerium sulfate solution, it is necessary to dilute the prepared cerium sulfate solution to different concentrations. According to the linear relationship between the absorbance of cerium sulfate solution at 316 nm and the concentration of  $Ce^{4+}$  (~0.05–0.6 mM), the concentration of  $H_2O_2$  of the sample can be obtained. The size of carbon paper is  $1*3\ cm^2$ . Add 50  $\mu l$  of catalyst ink to carbon paper and ensure that the load is  $1\ cm^2$ . Before electrolysis, inject oxygen into the cathode for at least 25 min to ensure oxygen saturation and maintain  $O_2$  in the electrolyte during measurement to ensure that the concentration of dissolved  $O_2$  remains stable.



The concentration of  $\text{H}_2\text{O}_2$  (M) can be determined by Eq.5:

$$M = 2 M \text{ Ce}^{4+} \quad (\text{Eq.5})$$

The stability test of  $\text{H}_2\text{O}_2$  was carried out in a H-type two-chamber electrolytic cell. The carbon paper with a catalyst load of  $0.5 \text{ mg cm}^{-2}$  was electrolyzed at an  $\text{O}_2$ -saturated cathode. The stability test was carried out at a magnetic stirring speed of 400 rpm and  $-0.4 \text{ V vs RHE}$ .

### DFT calculation

We performed spin-polarized density functional theory (DFT) calculations by the cestap code within the Materials Studio software package.<sup>1</sup> Interactions of the electrons were described by the Perdew–Burke–Ernzerhof (PBE) exchange–correlation function of the generalized gradient approximation (GGA).<sup>2</sup> The empirical correction in the Grimme scheme was used to describe the van der Waals interactions.<sup>3</sup> In the process of geometry optimizations, the convergence criteria of  $1 \times 10^{-6}$  Hartree was set for energy,  $0.002 \text{ Hartree/\AA}$  was set for the force, and  $0.005 \text{ \AA}$  was set for displacement. The convergence criterion of self-consistent field (SCF) computations was set for  $10^{-6}$  Hartree.  $0.005 \text{ Hartree}$  was set to the value of smearing to speed up convergence.

As shown by the XRD patterns, the (0 0 2), (2 0 0), (2 0 0) crystal facets were used to model the ZnO, NiO and CoO surfaces, respectively. The ZnO (0 0 2) was modeled as a 3-layered ( $2 \times 2$ ) slab, the NiO (2 0 0) was modeled as a 3-layered ( $2 \times 2$ ) slab, and the CoO (2 0 0) was modeled as a 3-layered ( $2 \times 2$ ) slab. The bottom layer was fixed while the top two layers were fully relaxed. A vacuum layer of  $15 \text{ \AA}$  was used to prohibit the periodic interactions of the slabs.

The Gibbs free energy change ( $\Delta G$ ) along the ORR was obtained by the computational hydrogen electrode (CHE) model. In this model, the chemical potential of the  $\text{H}^+/\text{e}^-$  pair is equal to half of the gas-phase  $\text{H}_2$  at standard hydrogen electrode (SHE) conditions. When an electron is transferred, the electrode potential ( $U$ ) is considered by shifting the electron by  $-eU$ .  $\Delta G$  was defined as:  $\Delta G = \Delta E + \Delta ZPE - T \Delta S + eU$ , where  $\Delta E$ ,  $\Delta ZPE$  and  $\Delta S$  denote

the energy difference between the products and the reactants, and the zero energy and entropy difference between the products and the reactants, respectively.  $e$  denotes the number of electrons transferred in the reaction;  $U$  represents the applied electrode potential. It is well known that the energy of  $O_2$  cannot be precisely calculated by the DFT approach. Therefore, we used free energy change of the reaction  $2H_2 + O_2 \rightarrow 2H_2O$  to obtain the free energy of  $O_2$ . Elementary step with a maximum free energy change during the reaction is identified as the potential-limiting step (PDS).

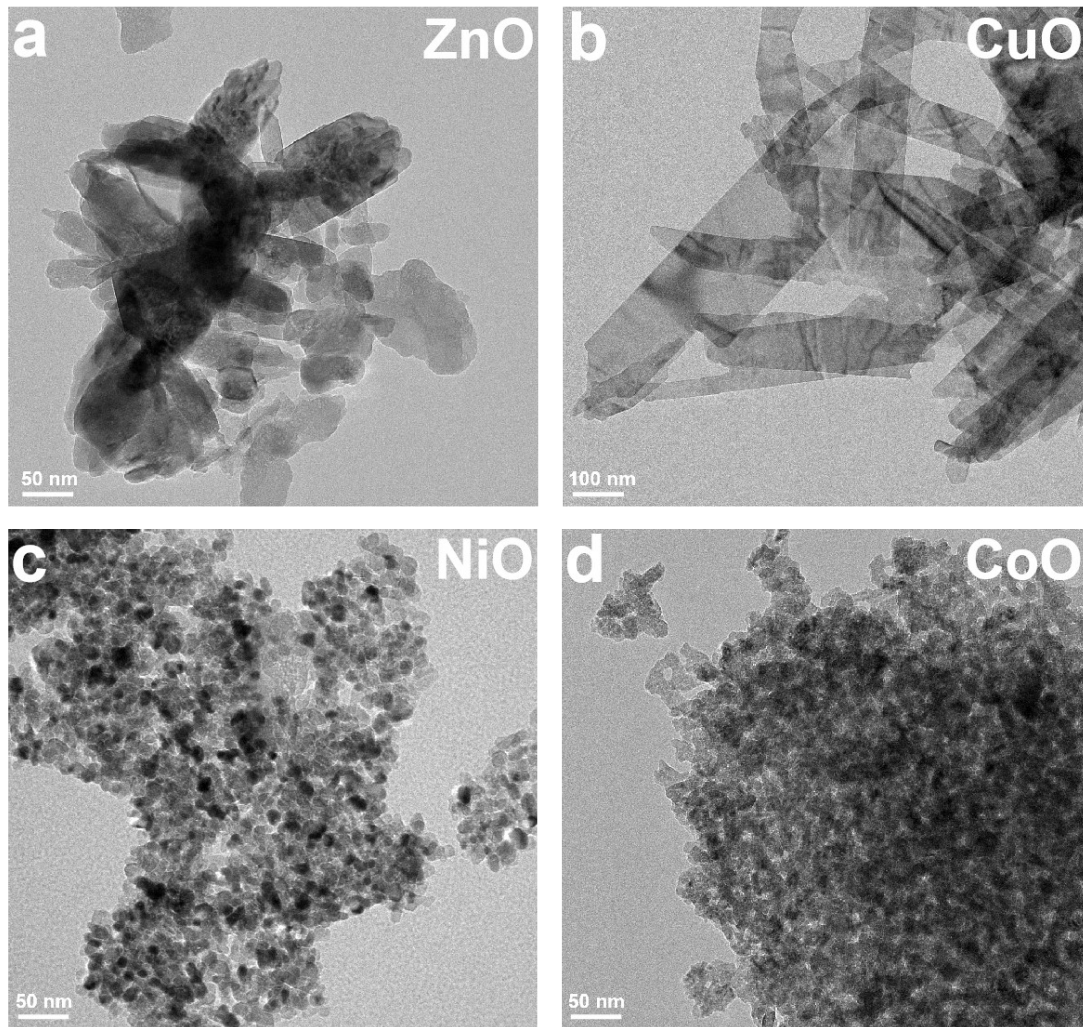


**Fig. S1** HRTEM image of (a) ZnO; (b) CuO; (c) NiO and (d) CoO.

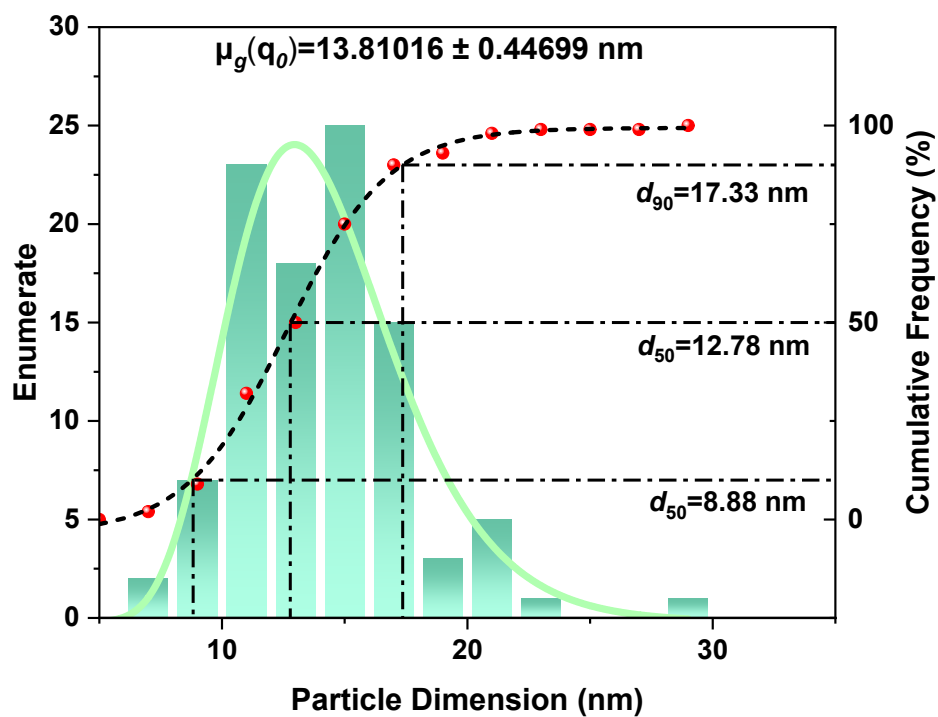
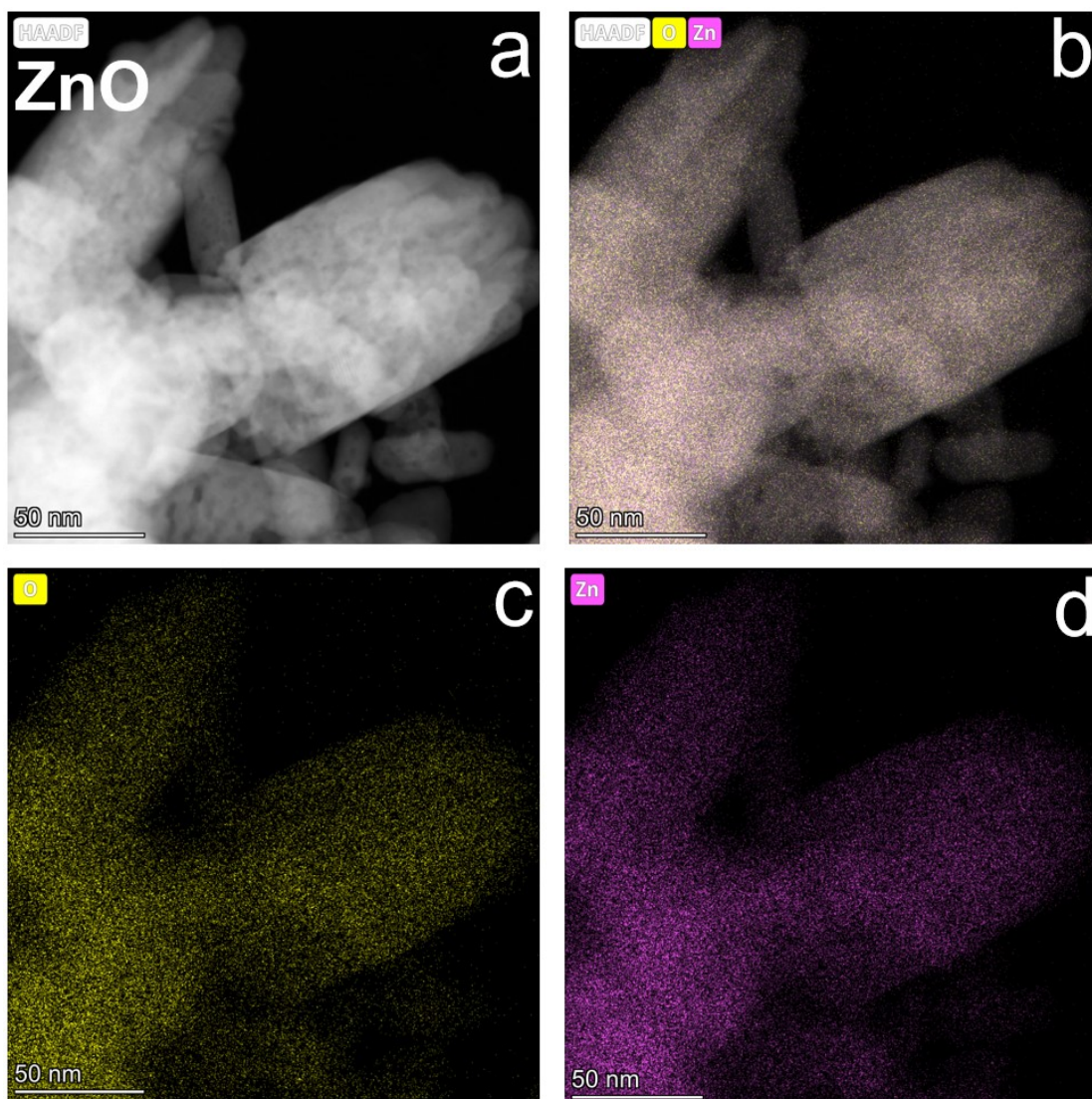
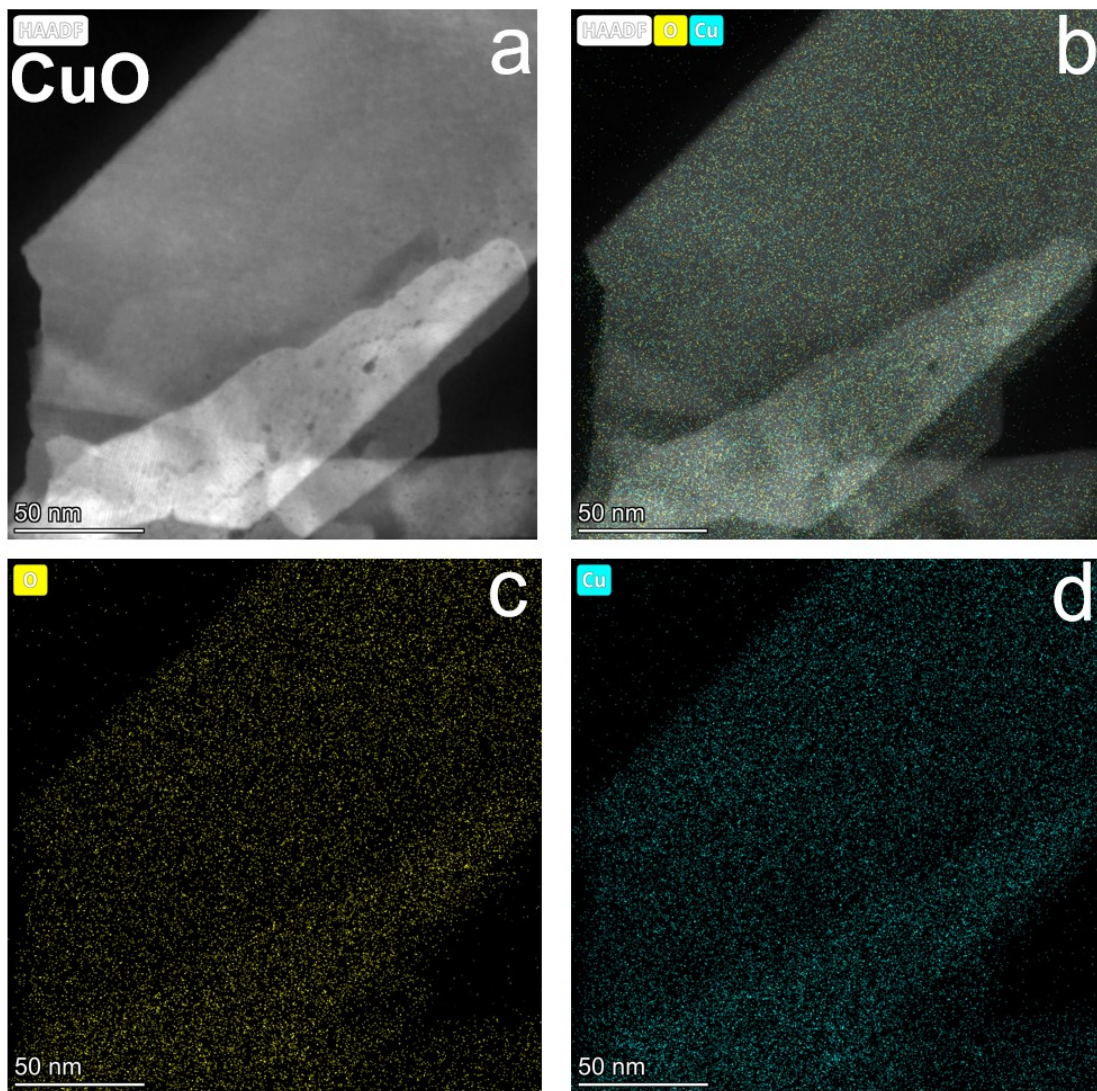


Fig. S2 Particle size distribution diagram drawn according to TEM image of NiO.



**Fig. S3** Corresponding elemental mapping of ZnO.



**Fig. S4** Corresponding elemental mapping of CuO.

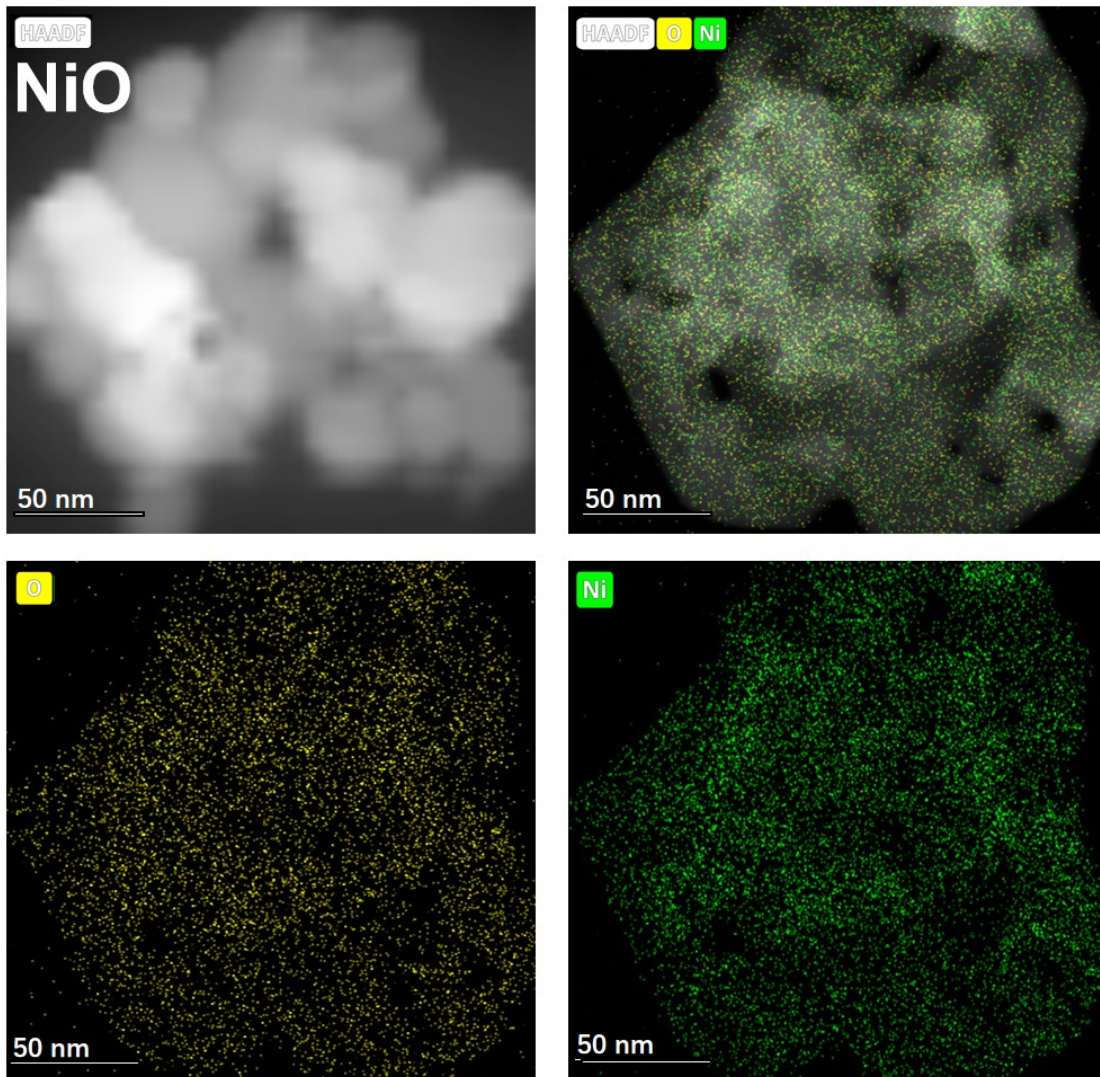


**Fig. S5** Corresponding elemental mapping of NiO.

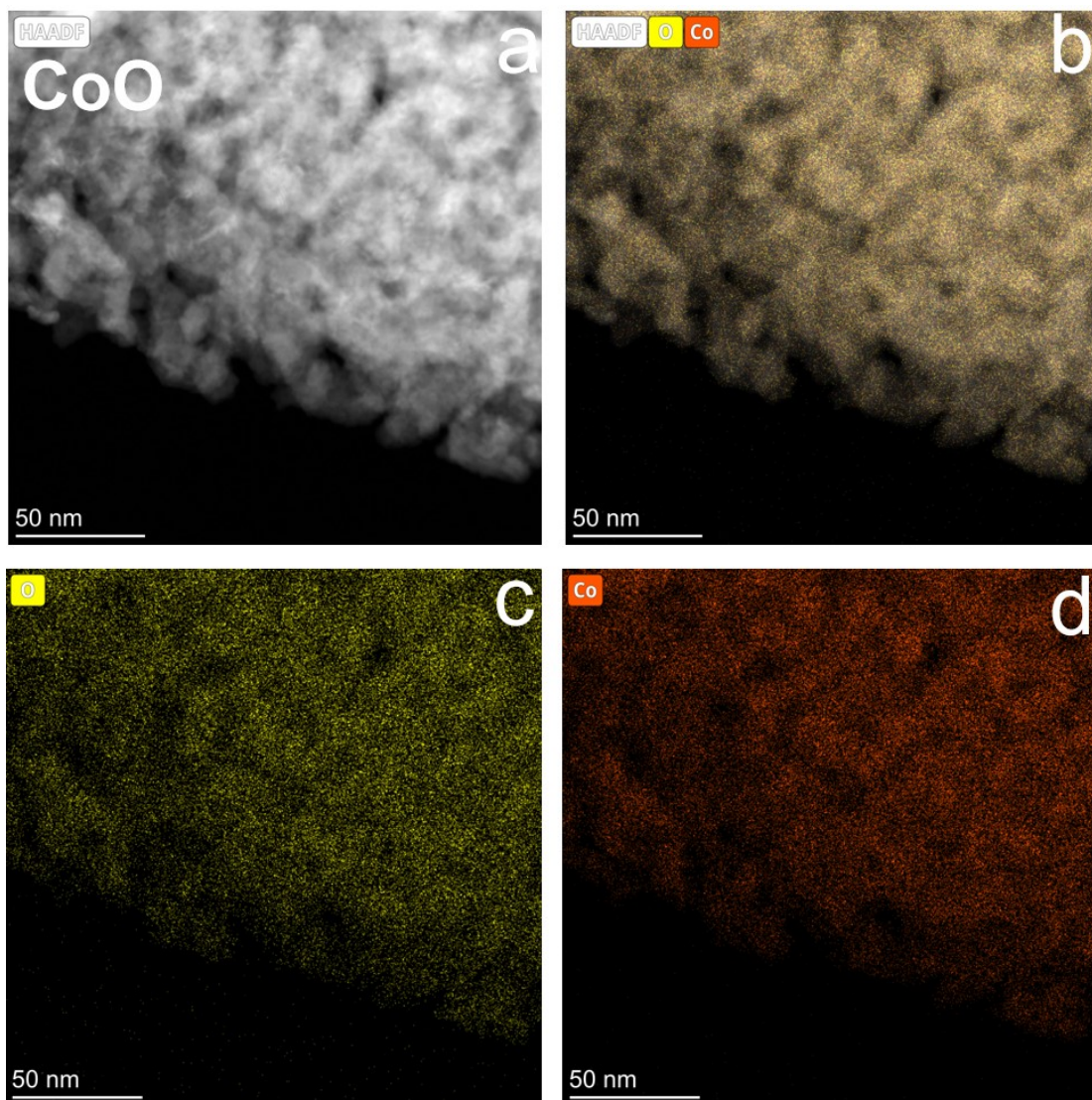


**Fig. S6** Corresponding elemental mapping of CoO.

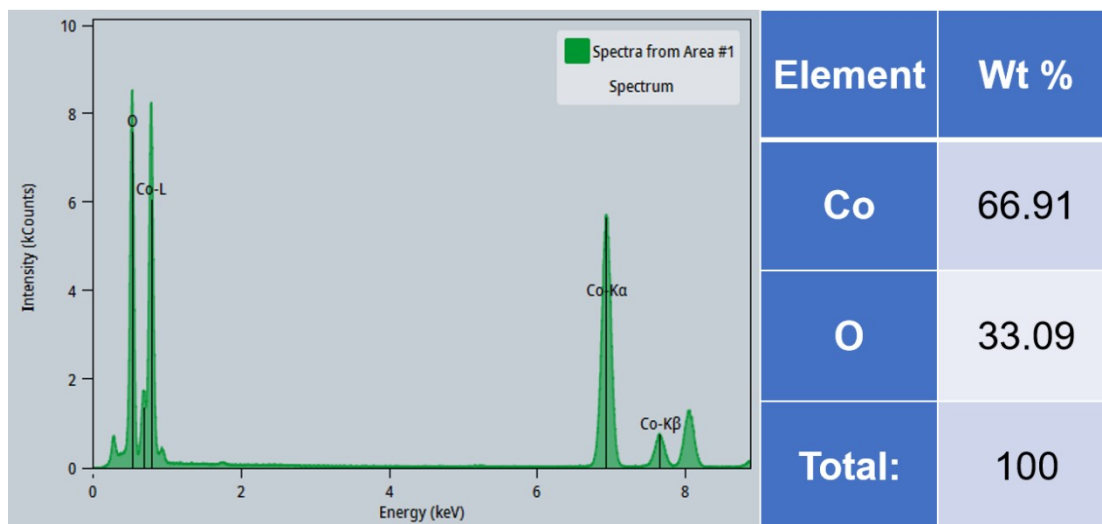


**Fig. S7** TEM-EDS image of CoO.

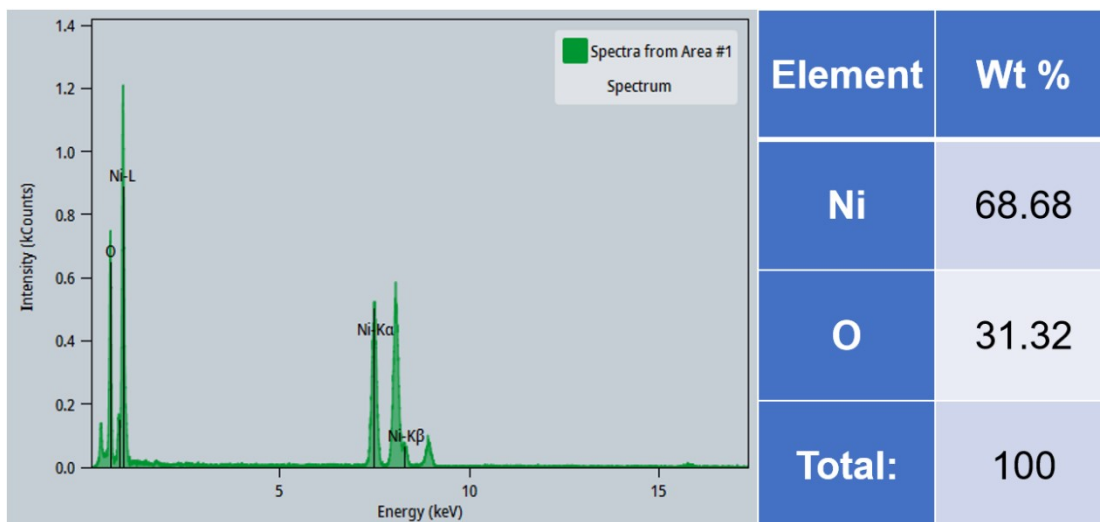


**Fig. S8** TEM-EDS image of NiO.

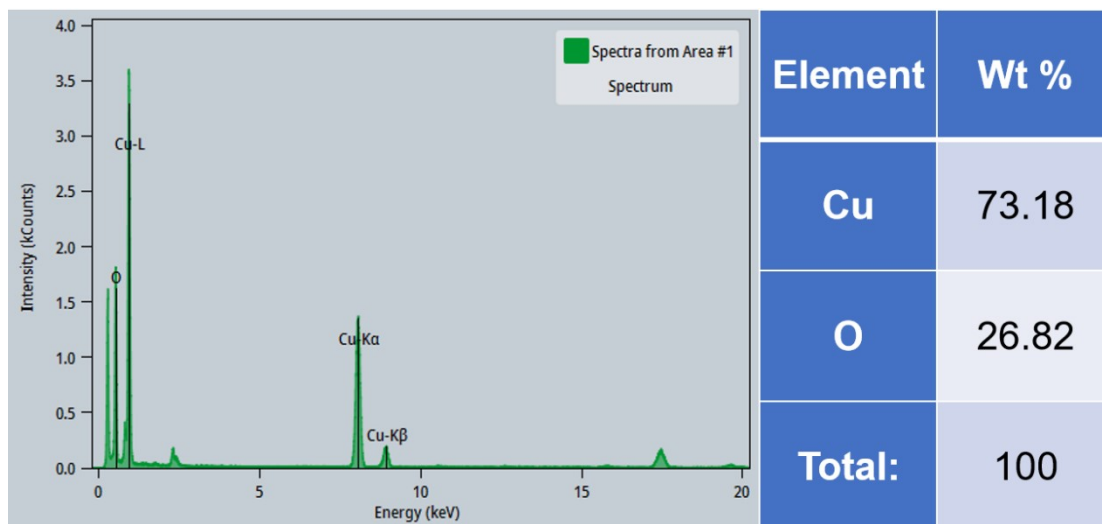


**Fig. S9** TEM-EDS image of CuO.

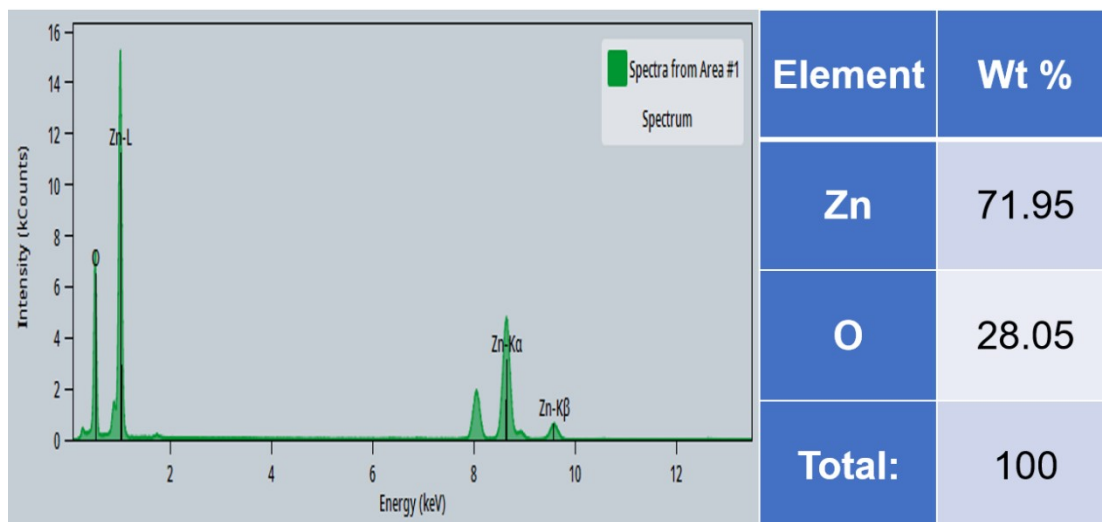


**Fig. S10** TEM-EDS image of ZnO.

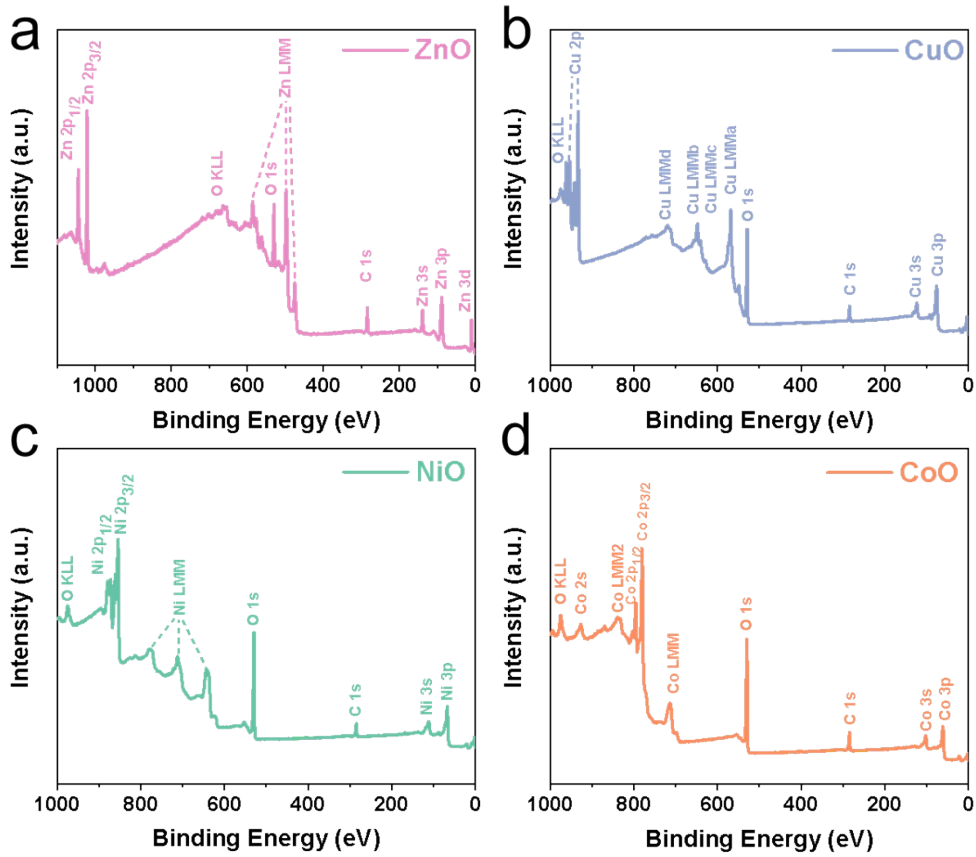


**Fig. S11** XPS survey spectra of (a) ZnO; (b) CuO; (c) NiO and (d) CoO.

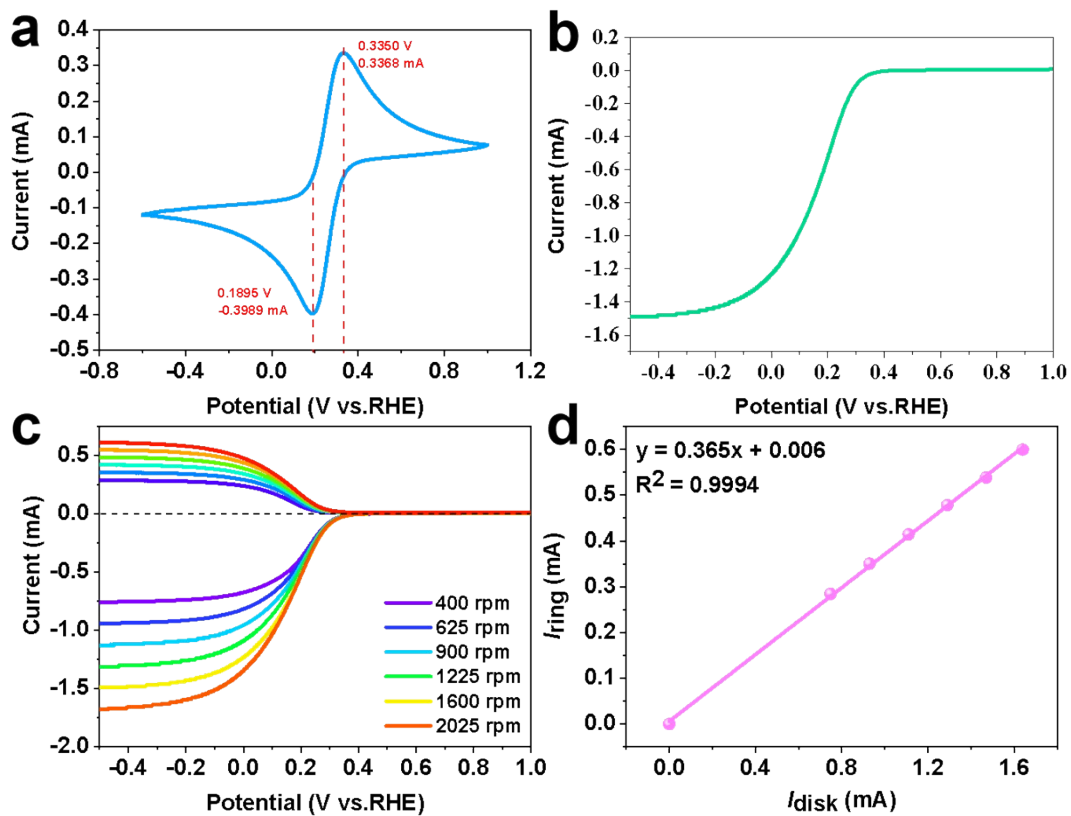


**Fig. S12** Calibration of the collection efficiency of the bare RRDE in  $N_2$  saturated electrolyte containing 0.329g  $K_3[Fe(CN)_6]$  and 7.455g KCl. (a) CV voltammetry of RRDE naked gas disk at 100mV /s. (b) LSV curve of Pt ring in 0.5 V vs. RHE at 100 mV/s and 1600 rpm. (c) RRDE voltammograms recorded at different rotation rates by performing LSV on the disk at 100 mV/s. (d) The corresponding collection efficiency of RRDE voltammograms as a function of the potential. All potentials in this figure are presented without iR-correction.

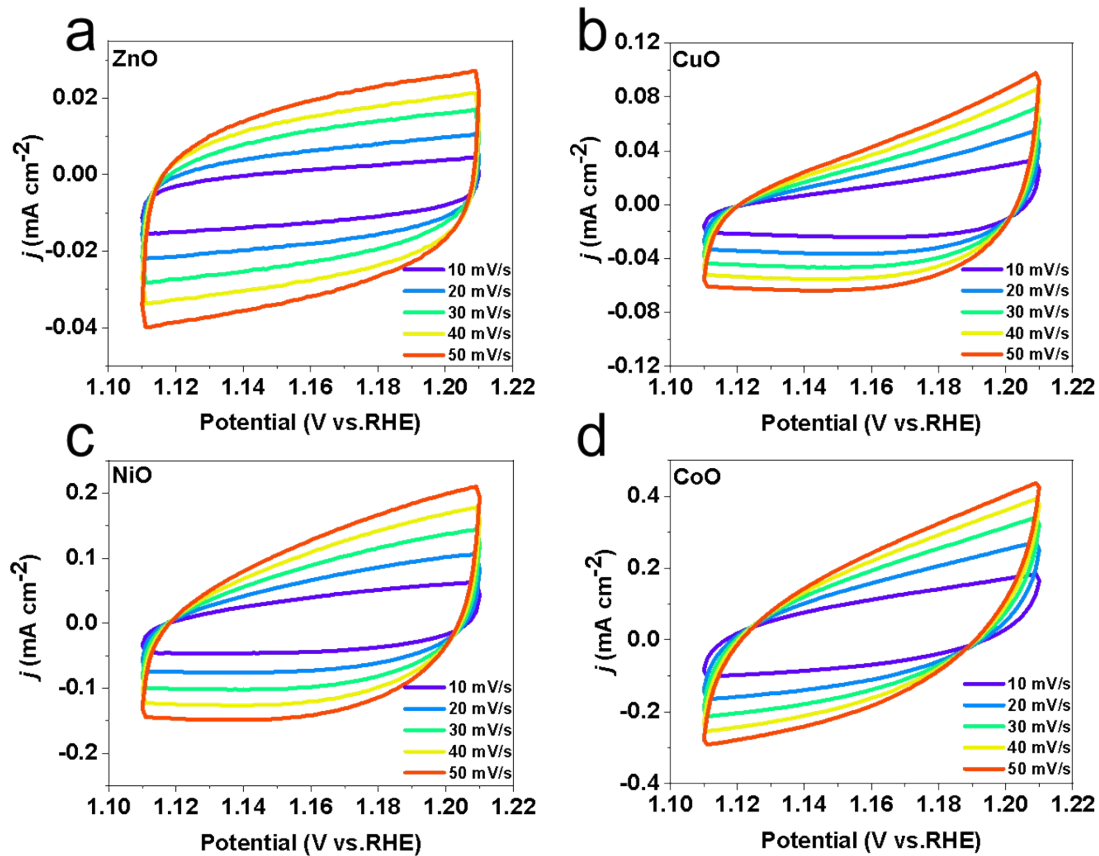


Fig. S13 CV curves in the potential range of 1.11-1.21V vs. RHE: (a) ZnO, (b) CuO, (c) NiO and (d) CoO. (Synthetic samples with slightly different sizes)

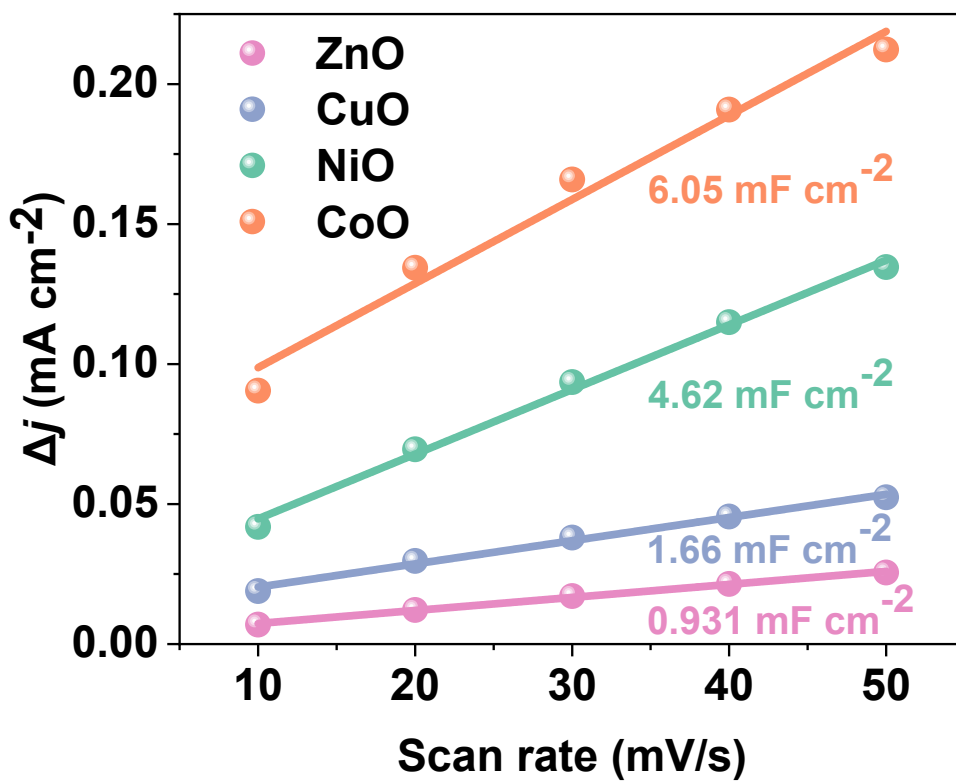


Fig. S14 Current density differences plotted against scan rate of ZnO, CuO, NiO and CoO.(Synthetic samples with slightly different sizes)

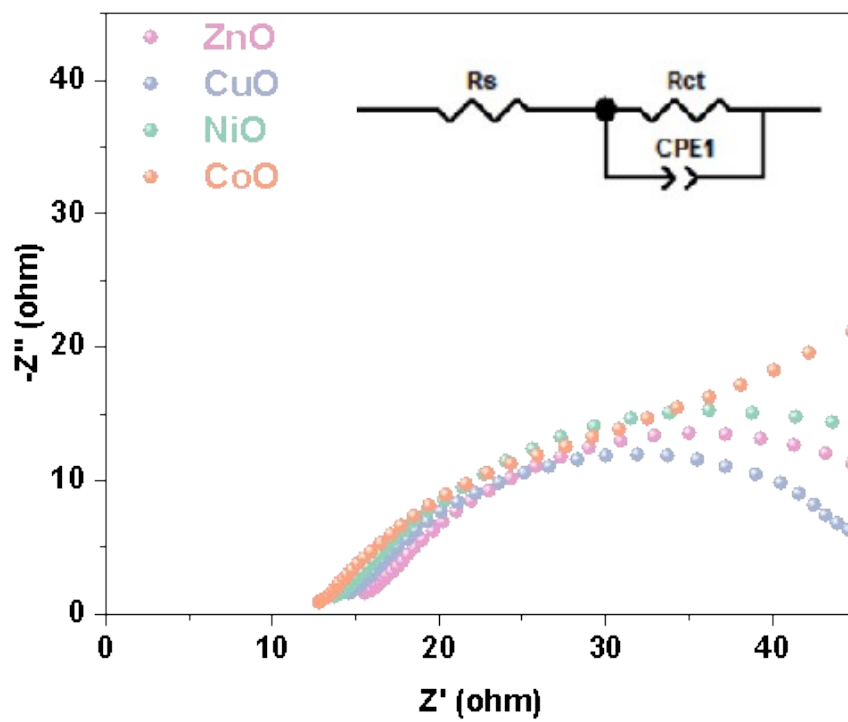
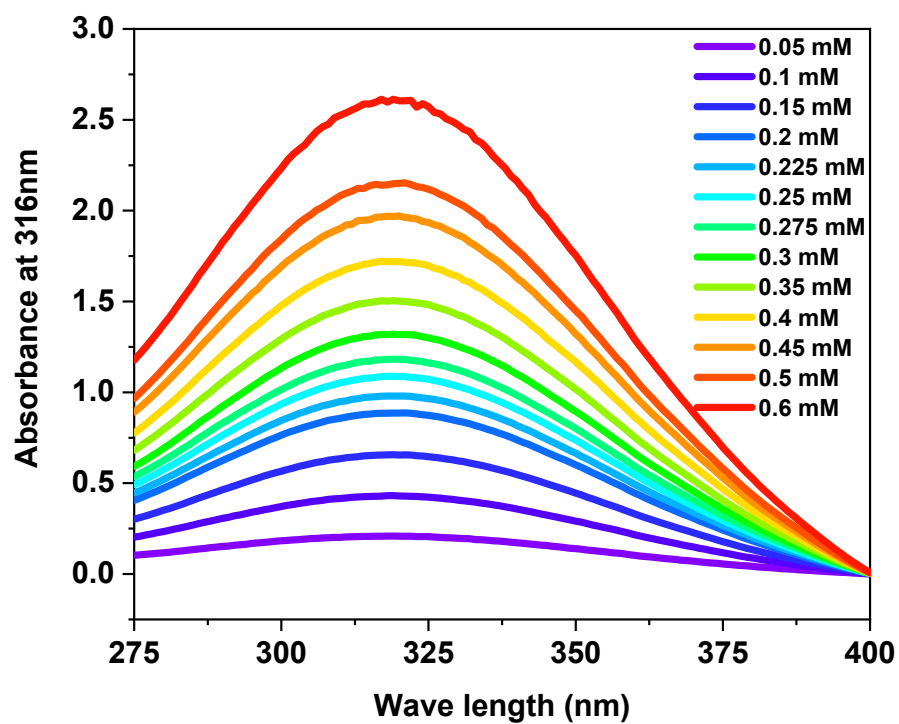
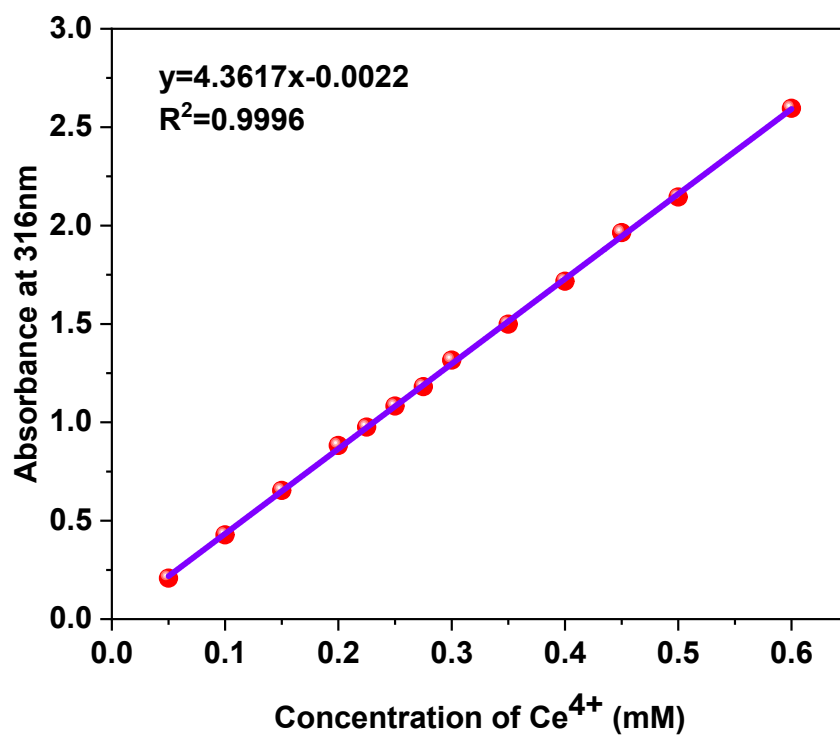


Fig. S15 Electrochemical impedance spectra of ZnO, CuO, NiO and CoO.



**Fig. S16** Absorbance spectra of standard  $\text{Ce}(\text{SO}_4)_2$  solutions (up to 0.6 mM) in  $0.5 \text{ M H}_2\text{SO}_4$ .



**Fig. S17** Linear relationship between absorbance and cerium sulfate solution with different concentration.

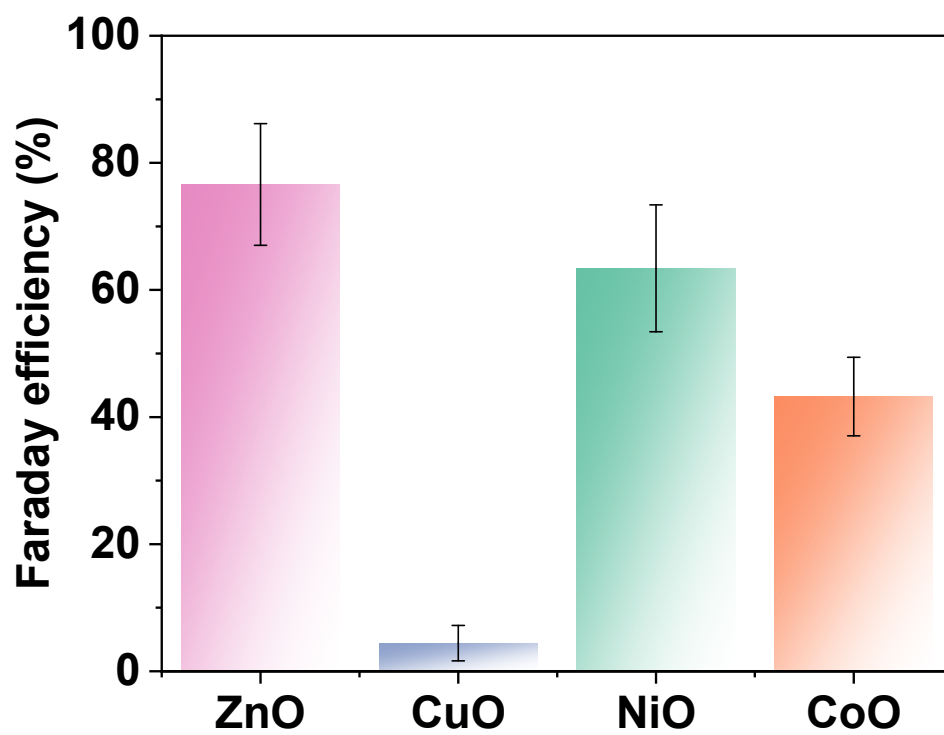


**Fig. S18** Faraday efficiency after 5 cycles at 7200s in 0.1 M KOH solution.

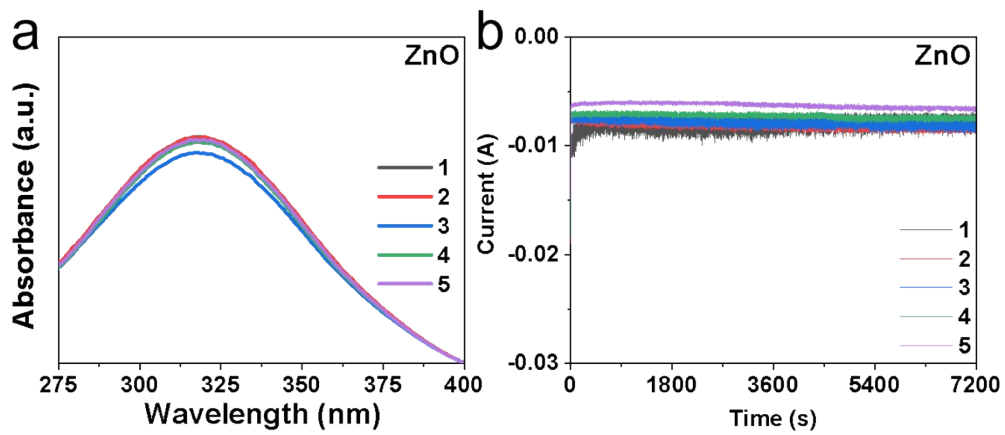


Fig. S19 The current stability curve and the yield curve of  $H_2O_2$  of ZnO.

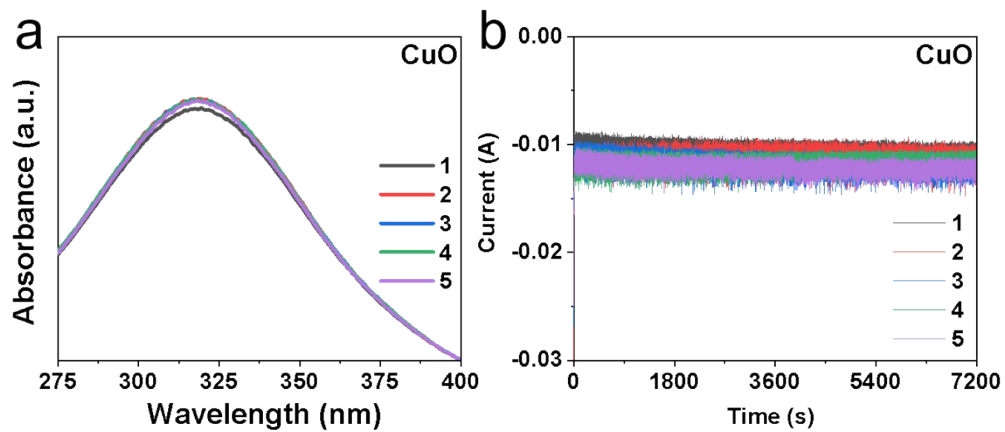


Fig. S20 The current stability curve and the yield curve of  $H_2O_2$  of CuO.

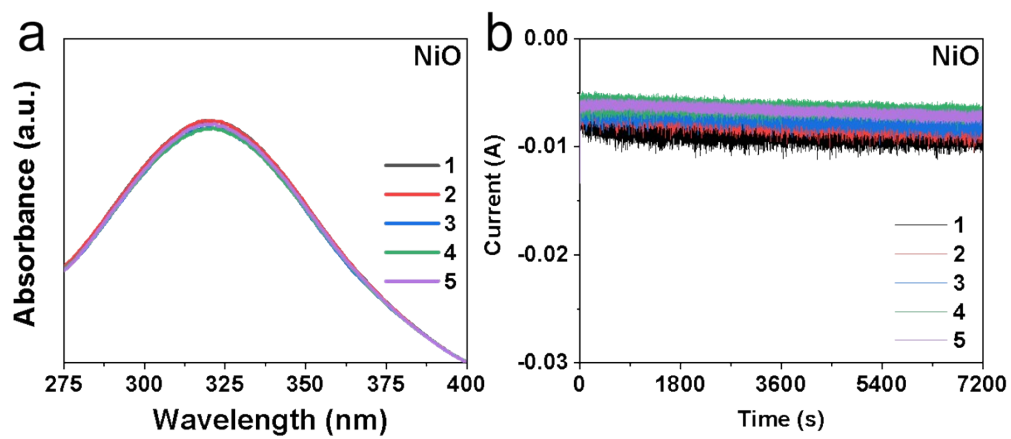


Fig. S21 The current stability curve and the yield curve of  $\text{H}_2\text{O}_2$  of NiO.

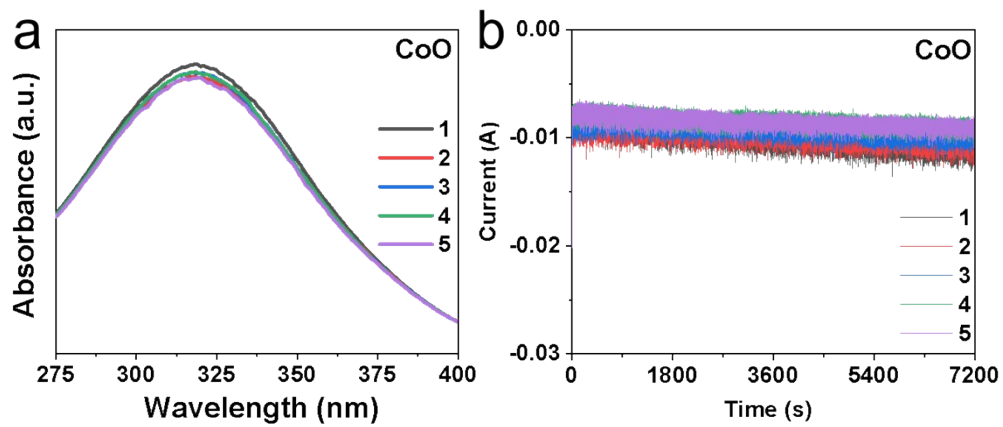
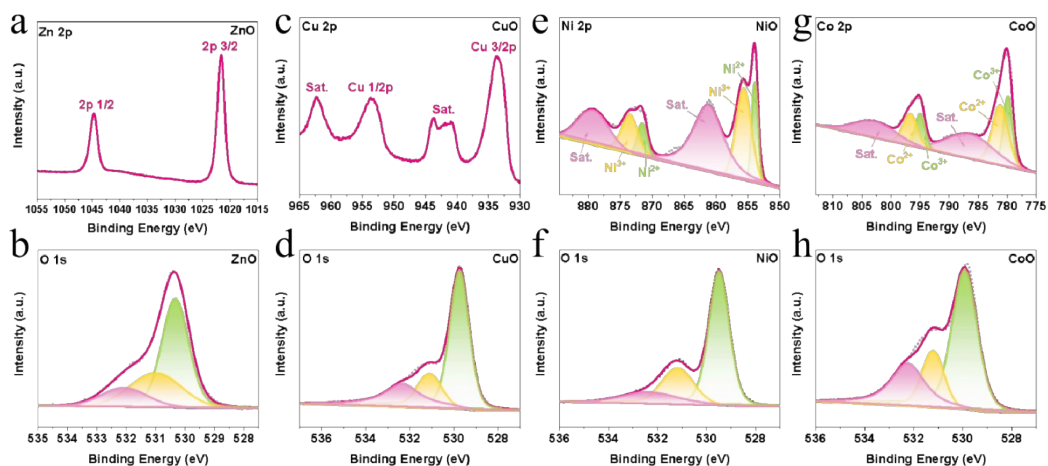
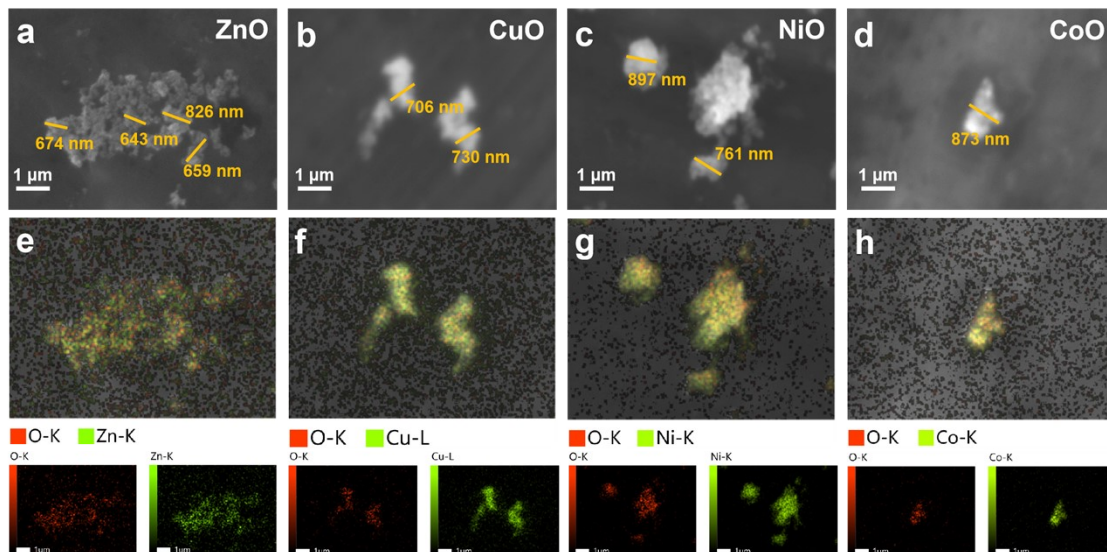


Fig. S22 The current stability curve and the yield curve of  $H_2O_2$  of CoO.



**Fig. S23** The high-resolution XPS spectra of (a) Zn 2p spectra and (b) O 1s spectra of ZnO; (c) Cu 2p spectra and (d) O 1s spectra of CuO; (e) Ni 2p spectra and (f) O 1s spectra of NiO and (g) Co 2p spectra and (h) O 1s spectra of CoO, after 5 cycles, with a total duration of 7200 s, in 0.1 M KOH solution.



**Fig. S24** (a), (b), (c) and (d) are scanning electron microscope images of purchased ZnO, CuO, NiO and CoO, respectively; (e), (f), (g) and (h) are the corresponding element maps of purchased ZnO, CuO, NiO and CoO, respectively.

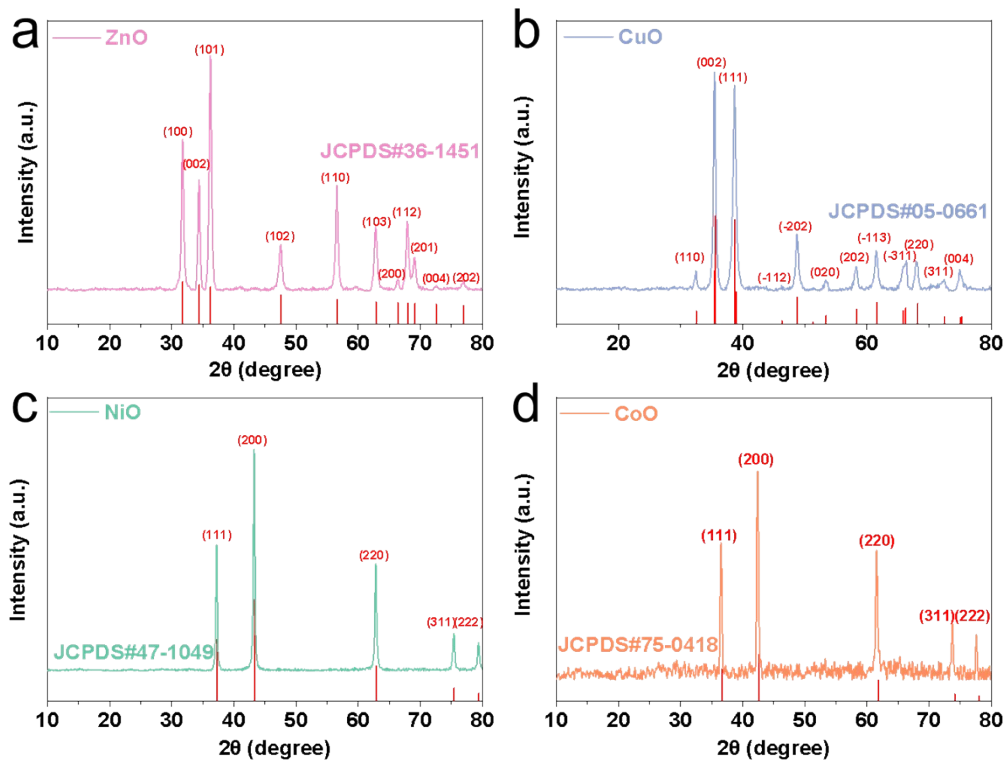
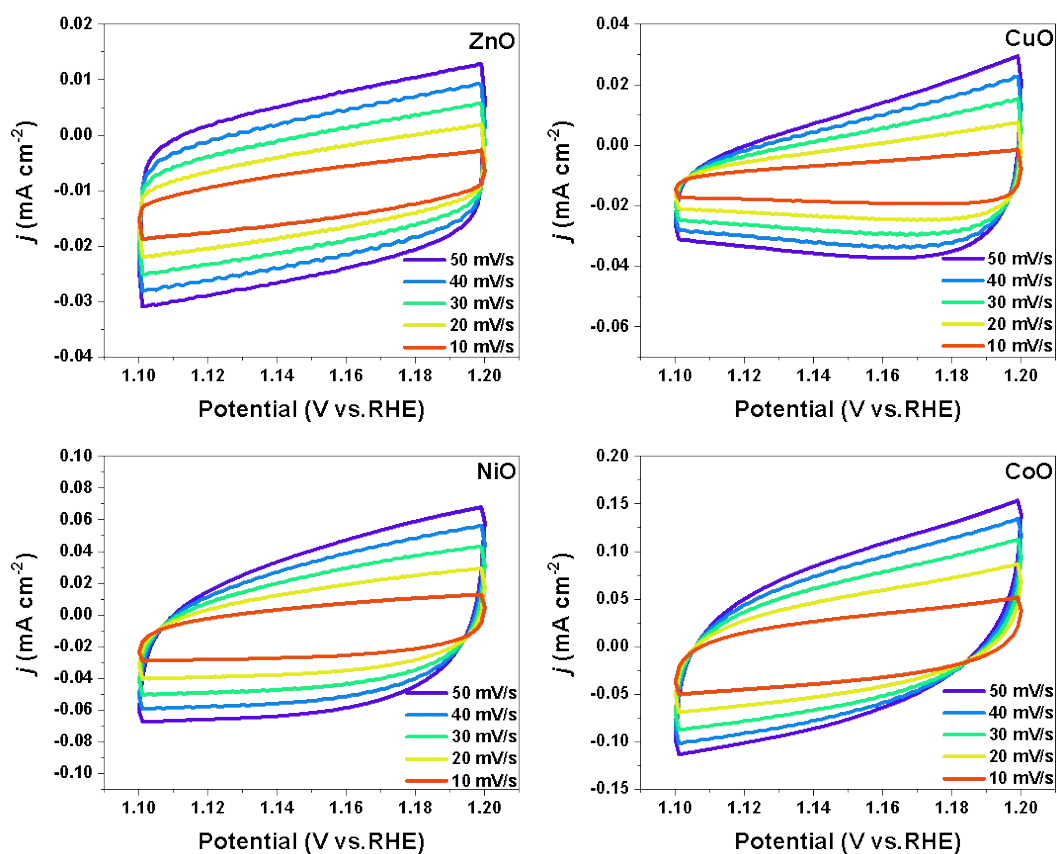
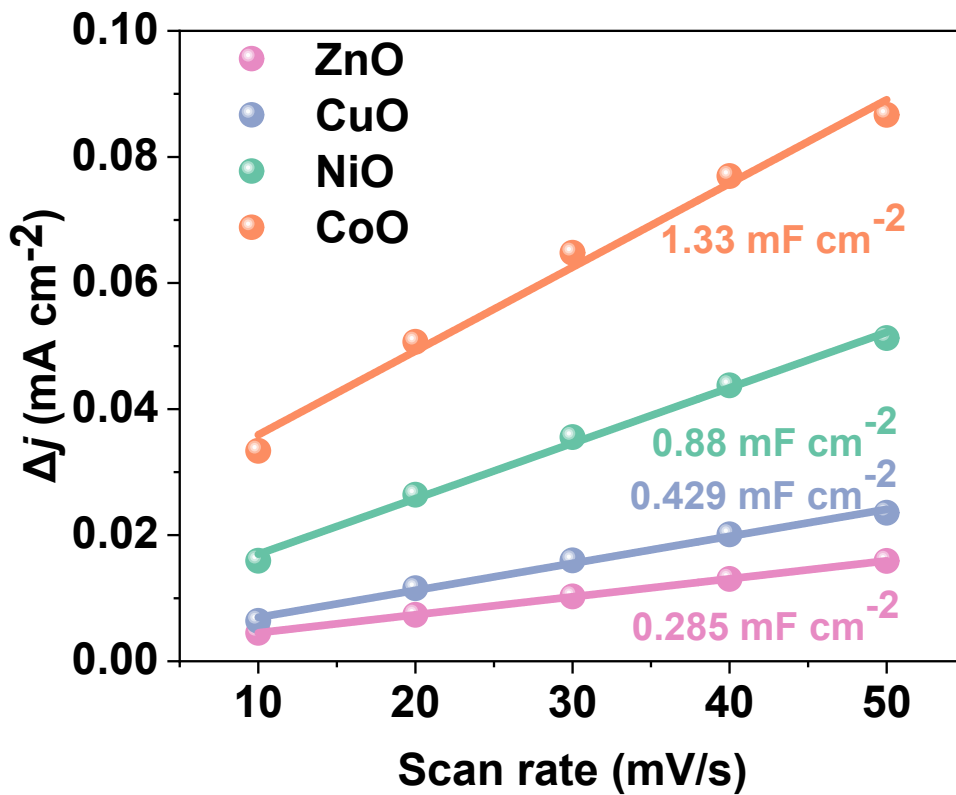


Fig. S25 XRD pattern of (a) ZnO (b) CuO, (c) NiO and (d) CoO of purchase size close.



**Fig. S26** CV curves of (a) ZnO, (b) CuO, (c) NiO and (d) CoO in the potential range of 1.11-1.21 V vs. RHE. (Samples are purchased in similar sizes.)



**Fig. S27** Current density differences plotted against scan rate of ZnO, CuO, NiO and CoO. (Samples are purchased in similar sizes.)

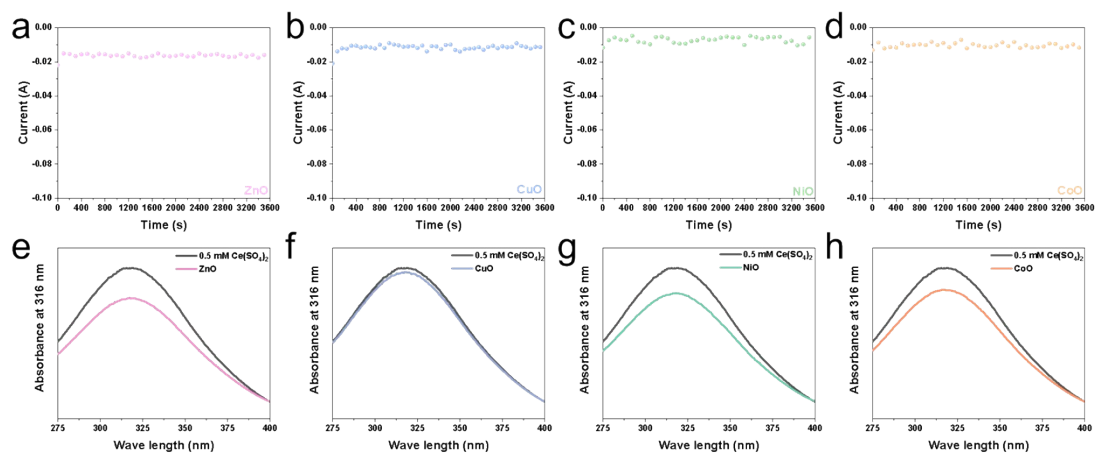


**Fig. S28** (a), (b), (c) and (d) are the current stability curves of ZnO, CuO, NiO and CoO with similar sizes; (e), (f), (g) and (h) are H<sub>2</sub>O<sub>2</sub> yield curves of ZnO, CuO, NiO and CoO with similar sizes.

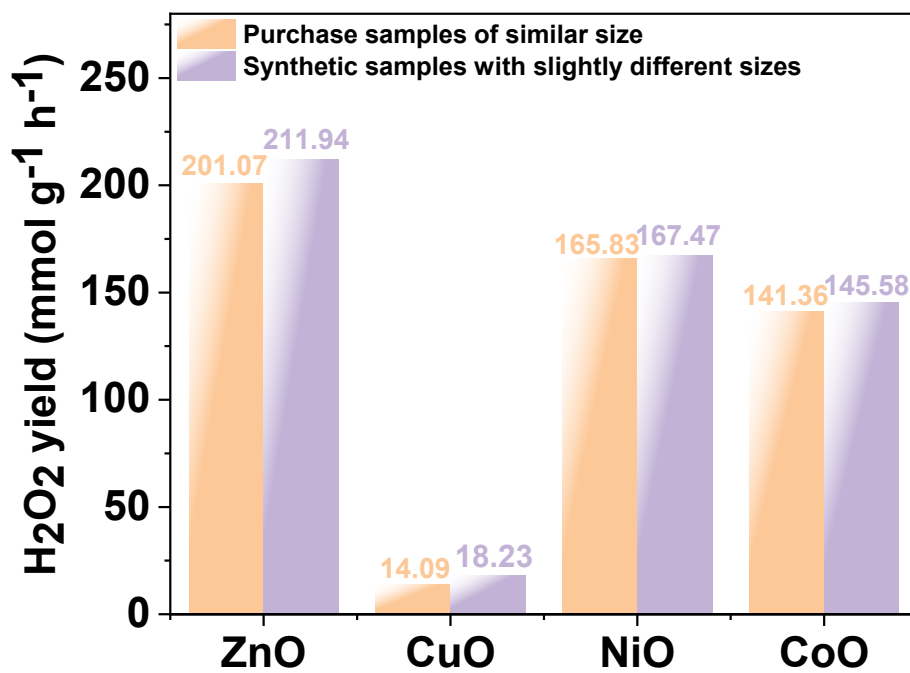


**Fig. S29** Comparison of hydrogen peroxide yield between purchased samples with similar size and synthetic samples with slightly different size.

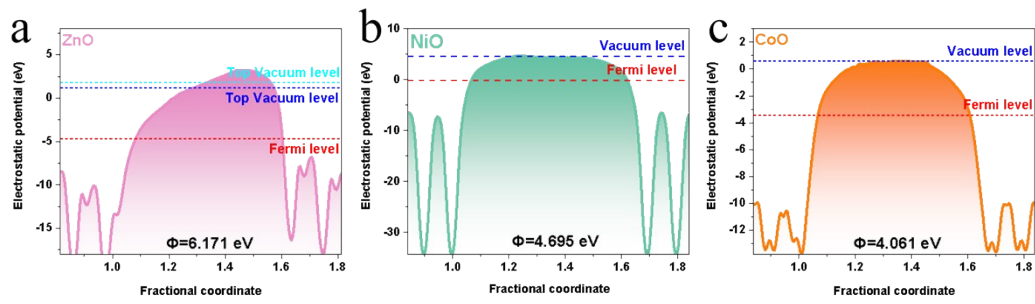


Fig. S30 Calculation work function of ZnO, NiO and CoO.

Table.S1 The elemental contents of CoO, NiO, CuO and ZnO were measured by XPS data.

Sample	Element content		
CoO	Co (at. %)	O (at. %)	C (at. %)
	26.89	52.98	20.13
NiO	Ni (at. %)	O (at. %)	C (at. %)
	38.58	46.42	15
CuO	Cu (at. %)	O (at. %)	C (at. %)
	37.32	44.79	17.89
ZnO	Zn (at. %)	O (at. %)	C (at. %)
	28.36	38.98	32.65

Table S2. The comparison of ORR activity of ZnO、CuO、NiO and CoO with those of recently reported ORR catalysts in alkaline solution.

Catalyst	Electryte	Selectivity@potential (%@V vs. RHE)	Productivity	Ref.
ZnO	0.1 M KOH	90.4@0.4	211.94mmol g <sup>-1</sup> h <sup>-1</sup>	
CuO	0.1 M KOH	82.8@0.4	18.23 mmol g <sup>-1</sup> h <sup>-1</sup>	This work
NiO	0.1 M KOH	79.4@0.4	167.47mmol g <sup>-1</sup> h <sup>-1</sup>	
CoO	0.1 M KOH	36.8@0.4	145.58mmol g <sup>-1</sup> h <sup>-1</sup>	
h-WO <sub>3</sub>	0.1 M KOH	71@0.4	128 mmol g <sup>-1</sup> h <sup>-1</sup>	
γ-WO <sub>3</sub>	0.1 M KOH	78@0.4	145 mmol g <sup>-1</sup> h <sup>-1</sup>	4
oxo-G/H <sub>2</sub> O <sub>2</sub> /NH <sub>3</sub> ·H <sub>2</sub> O	0.1 M KOH	82@0.4	224.8 mmol g <sup>-1</sup> h <sup>-1</sup>	5
Co-POC-O	0.1 M KOH	80@0.5	/	6
Fe <sub>3</sub> O <sub>4</sub> /graphene	1 M KOH	68@0.4	/	7
Fe <sub>3</sub> O <sub>4</sub> /Printex	1 M KOH	62@0.4	/	7
Nb <sub>2</sub> O <sub>5</sub> -rGO	0.1M NaOH	74.9@-0.4V vs Ag/AgCl	/	8
5.5% CeO <sub>2</sub> HARN/C	1 M NaOH	49@0.3	/	9
CuO <sub>x</sub> /graphene	1M KOH	~80%@0.6	/	10
Sr <sub>0.7</sub> Na <sub>0.3</sub> SiO <sub>3-δ</sub>	0.1 M KOH	65-82@0.3-0.6	/	11
Mo-TiO <sub>2</sub>	0.1 M KOH	86@0.68	395.3 mmol g <sub>cat</sub> <sup>-1</sup> h <sup>-1</sup>	12
TiO <sub>2</sub>	0.1 M KOH	52@0.62	~140 mmol g <sub>cat</sub> <sup>-1</sup> h <sup>-1</sup>	12
Ta <sub>2</sub> O <sub>5</sub> /C	0.1 M K <sub>2</sub> SO <sub>4</sub>	83.2@-0.5V vs Ag/AgCl	/	13
V <sub>x</sub> O <sub>y</sub> /C	1 M NaOH	68@0.4	/	14

## References

1. B. Delley, *Journal of Chemical Physics*, 2000, **113**, 7756-7764.
2. J. P. Perdew, K. Burke and M. Ernzerhof, *Physical Review Letters*, 1996, **77**, 3865-3868.
3. S. Grimme, *Journal of Computational Chemistry*, 2006, **27**, 1787-1799.
4. H. Jiang, Y. Wang, J. Hu, X. Shai, C. X. Zhang, T. Q. Y. Le, L. B. Zhang and M. H. Shao, *Chem. Eng. J.*, 2023, **452**, 139449.
5. L. Han, Y. Sun, S. Li, C. Cheng, C. E. Halbig, P. Feicht, J. L. Huebner, P. Strasser and S. Eigler, *Acs Catalysis*, 2019, **9**, 1283-1288.
6. B.-Q. Li, C.-X. Zhao, J.-N. Liu and Q. Zhang, *Advanced Materials*, 2019, **31**.
7. W. R. P. Barros, Q. Wei, G. Zhang, S. Sun, M. R. V. Lanza and A. C. Tavares, *Electrochimica Acta*, 2015, **162**, 263-270.
8. J. F. Carneiro, M. J. Paulo, M. Siaj, A. C. Tavares and M. R. V. Lanza, *Journal of Catalysis*, 2015, **332**, 51-61.
9. V. S. Pinheiro, E. C. Paz, L. R. Aveiro, L. S. Parreira, F. M. Souza, P. H. C. Camargo and M. C. Santos, *Electrochimica Acta*, 2018, **259**, 865-872.
10. H. Xiao, B. Li, M. Zhao, Y. Li, T. J. Hu, J. F. Jia and H. S. Wu, *Chemical Communications*, 2021, **57**, 4118-4121.
11. S. Thundiyil, S. Kurungot and R. N. Devi, *Acs Applied Materials & Interfaces*, 2021, **13**, 382-390.
12. Z. Q. Deng, C. Q. Ma, S. H. Yan, J. Liang, K. Dong, T. S. Li, Y. Wang, L. C. Yue, Y. L. Luo, Q. Liu, Y. Liu, S. Y. Gao, J. Du and X. P. Sun, *Catal. Sci. Technol.*, 2021, **11**, 6970-6974.
13. J. F. Carneiro, R. S. Rocha, P. Hammer, R. Bertazzoli and M. R. V. Lanza, *Applied Catalysis a-General*, 2016, **517**, 161-167.
14. A. Moraes, M. H. M. T. Assumpcao, R. Papai, I. Gaubeur, R. S. Rocha, R. M. Reis, M. L. Calegari, M. R. V. Lanza and M. C. Santos, *Journal of Electroanalytical Chemistry*, 2014, **719**, 127-132.